Thermally Evaporated MoO3 Nanowires as Oxygen Evolution Reaction Catalysts for Water Splitting Applications

ACS APPLIED NANO MATERIALS, vol. 6, 2023, 22947 - 22955

published with DOI: 10.1021/acsanm.3c04288

Thermally-Evaporated MoO_3 Nanowires as OER Catalyst for Water Splitting Applications

S. Scalese[1,*], F. Tringali[2, 3], A. Lo Mastro[2, 3], S. La Manna[2, 3], G. Mineo[2,3], A. Russo[2], M. Scuderi[1], M. Miritello[3], G. Franzò[3], S. Mirabella[2, 3] and A. Terrasi[2, 3]

[1] Istituto per la Microelettronica e Microsistemi - Consiglio Nazionale delle Ricerche (CNR-IMM), Ottava Strada n.5, I-95121 Catania, Italy
[2] Dipartimento di Fisica e Astronomia, Università degli Studi di Catania, via S. Sofia 64, I-95123 Catania, Italy
[3] Istituto per la Microelettronica e Microsistemi - Consiglio Nazionale delle Ricerche (CNR-IMM), sede di Catania—Università, via S. Sofia 64, I-95123 Catania;

**Corresponding author; e-mail: silvia.scalese@imm.cnr.it*

Abstract

In this work we report the growth of MoO_3 nanowires (NWs) by thermal evaporation with the aim of evaluating their use as catalysts for oxygen evolution reaction (OER) in water splitting application. Growth was performed on two different kinds of substrates, Si(100) and Si(111), and at different growth temperatures between 200°C and 400°C, and the effect of such experimental parameters on the morphological, structural and compositional properties was investigated. The deposited materials were characterized by in situ Reflection High Energy Electron diffraction (RHEED), scanning electron microscopy (SEM), transmission electron microscopy (TEM), Rutherford Backscattering spectroscopy (RBS), X-ray Diffraction (XRD). For a growth temperature of 200°C a flat and amorphous oxide layer is obtained, while as the temperature is increased 1D growth prevails on 2D layer formation. In particular, at 400°C the deposited material consists of a high density array of MoO_3 crystalline NWs a few nm in diameter and up to about 0.5 μm in length. Only in the case of Si(111) substrates, small three-dimensional structures form and coexist with NWs since the beginning of the growth process.

Finally, oxygen evolution reaction (OER) activity of MoO_3 NWs was evaluated. The nanostructures were deposited on graphene paper and their electrochemical activity was investigated and compared to other non-precious metal-based catalysts for alkaline OER. Our MoO_3 based electrodes showed an overpotential of 330 mV and 340 mV at 10 mA/cm^2 (η_{10}) depending on the average length of NWs, and a quite high mass activity associated with a low catalyst loading, thus fitting the best performing electrocatalysts. Our results demonstrate that MoO_3 NWs are a suitable candidate for the development of anode electrodes for water splitting application.

Keywords: MoO_3 nanowires, Mo oxide phases, thermal evaporation, OER, electrocatalyst, water splitting

Introduction

Molybdenum oxide is an n-type semiconductor with interesting potentialities in several application fields, such as photovoltaics, electronics, catalysis, gas sensors, energy storage. Its properties and, therefore, its suitability for specific applications are strictly dependent on the synthesis methodology. For this reason, it is worthy to explore a variety of preparation methods to get Mo oxides with different stoichiometries, structures and dimensionality.

MoO_3 shows a wide energy band-gap (> 2.8 eV) and high work function (> 6.8 eV) and is stable in two crystalline phases, orthorhombic α-MoO_3 and monoclinic β-MoO_3, both featuring distinct and unique physical and chemical properties; along with them, under very specific conditions several other metastable phases have been reported, such as hexagonal h-MoO_3 and ε-MoO_3.

Countless nanostructures of molybdenum oxide are reported and optimized for several applications, differing in shape, size and structure, always taking advantage of the enhancement of aspect ratio, i.e. large active surface exposed. Xiao et al. [1] reported growth/esfoliation of MoO_3 nanosheets with high pseudocapacitive performances; Borah et al. synthesized MoO_3 quantum dots by sonication induced chemical etching of thin films [2]. Hydrothermal methods are among the most common techniques to produce MoO_3 NWs (and other kinds of nanostructures) with hexagonal phase [3] or orthorombic phase [4, 5]. Studies on MoO_3 NWs grown by thermal evaporation are limited. Only a few papers deal with MoO_3 grown by thermal evaporation, but they used metallic Mo source and obtained MoO_x structures that were successively oxidized to obtain Mo trioxide, like for example, in the work by Zhou et al. [6].

The methodology we propose here to obtain this kind of structures is quite different from what is already proposed in the literature and does not require two steps (Mo evaporation and oxidation). Furthermore, in this paper we report a catalyst-free mechanism of nanowires growth, which offers obvious benefits in terms of simplicity of the process. The absence of catalysts allows to prevent any unintentional contamination and to obtain pure nanowires. Furthermore, catalyst-free methods offer low-cost synthesis with fewer preparation steps, which is a prerequisite for high-yield nanowire production [7]. A similar methodology with respect to ours is the one used by Maiti et al., who observed MBE growth of β-MoO_3 nanoribbons with monoclinic phase on different substrates and investigated their field emission properties [8].

In general, the advantage coming from the use of nanostructures instead of bulk materials derives from the higher surface to volume ratio and can be exploited in any application requiring extended active interfaces, such as sensing and electrochemical water splitting.

In water splitting, oxygen evolution reaction (OER) is the next half-reaction of water splitting after hydrogen evolution reaction (HER). To produce O_2 molecules, a transfer of four electrons is required [9] and the entire oxygen evolution reaction process is given by multi-step reactions with transfer of single electron in each step [10], making OER kinetics quite slow with very large overpotential. This affects the formation of O=O bond occurring after the breaking of O-H bond. Therefore, there is an urgent requirement for an efficient, low cost OER electrocatalyst with low overpotential, high stability, durability. Among the various transition metal oxides, MoO_3 has been recently investigated because of its non-toxicity, excellent catalytic and electrochemical properties and low cost [11].

In this work we report the synthesis and characterization of extremely thin MoO_3 nanowires with a diameter of 10-15 nm and a length of hundreds of nanometers, resulting in superior surface to volume ratio and, finally, we evaluate their possible exploitation as OER catalysts for water splitting application. MoO_3 NWs were grown at 400°C and showed an orthorhombic structure, as observed by TEM and XRD analysis, whereas at lower temperatures an amorphous layer (200°C) or a layer with monoclinic phase (300°C) were formed.
Oxygen evolution reaction (OER) activity of orthorhombic MoO_3 NWs was evaluated, showing they have good electrocatalytic properties, making them a suitable candidate for the development of anode electrodes for water splitting application.

1. Experimental (Materials and Methods)

1.1 Growth

Deposition of molybdenum oxide was carried out via thermal evaporation in an ultra-high vacuum MBE system (DCA instruments, Turku, Finland). MoO_3 pellets (99,95% purity, as purchased from Neyco Vacuum and Materials) were placed in a 10 cc alumina crucible of an effusion cell (DCA instruments, Turku, Finland) equipped with a double heating filament. The effusion cell temperature is software controlled and monitored by a thermocouple during deposition process. Prior to the deposition, Si substrates (Si(100) and Si(111) 5 inches wafers) were cleaned according to the following steps: (1) UV-Ozone cleaning, with a wavelength of 253.7 nm, for 5 minutes by "Jelight UVO Cleaner Model 42"; (2) Chemical attack in Hydrofluoric Acid 2% aqueous solution for 1 minute; (3) Rinsing in DI water; (4) Baking in high vacuum inside the load lock chamber, 200°C for 20 minutes to remove adsorbed water. Once the load lock chamber vacuum is restored, the substrate is moved to the deposition chamber and heated up while rotating, in order to allow

surface reconstruction. After these steps, the substrate temperature is set to the desired temperature and the deposition process begins. The starting pressure in the chamber is in the range of 1.5-2 $\times 10^{-9}$ mbar, while the working pressures throughout the depositions vary depending on the temperature.

1.2 Materials characterization

Morphological and structural characterization of the samples was performed by scanning electron microscopy (SEM) in plan and cross section view, using a field emission scanning electron microscope (Supra35 FE-SEM by Zeiss, Oberkochen, Germany).

Transmission electron microscopy (TEM) was used for a nanoscale structural characterization of the NWs and was performed in a probe Cs-corrected JEM-ARM200F by JEOL (Akishima, Tokyo), equipped with a cold FEG operated at a primary beam energy of 200 keV in scanning TEM (STEM) mode. The as-synthesized NWs were transferred from the substrate directly on the TEM grid by mechanical rubbing.

X-ray diffraction (XRD) analysis was carried out for samples deposited on Si(100) at 200°C, 300°C and 400°C using a Smartlab Rigaku Diffractometer in Bragg-Brentano geometry, equipped with a rotating angle detector of Cu-K_α radiation operating at 45kV and 200mA. The instrument was operated at grazing incidence angle (0.5°) and data were collected with a 0.02° increment steps.

Rutherford Backscattering Spectrometry (RBS) was employed to probe the elemental depth distribution. He^{2+} ions are accelerated in a coaxial HVEE Singletron up to 2 MeV and focused into a high vacuum scattering chamber, where samples are placed onto a triaxial rotating stage. All the spectra were acquired for a total backscattered charge of 30 μC and analysed via xRUMP software to obtain quantitative information on samples elemental compositions.

1.3 Electrode preparation and electrochemical characterization

Nanowires were removed from the substrates after growth by sonication in isopropanol for a few minutes and the MoO_3 based electrodes were prepared by drop casting the MoO_3 NWs dispersion onto a graphene paper substrate (GP, 2x1 cm2, Sigma Aldrich, 240 μm thick) and by drying on hot plate at 60 °C for 30 minutes. A Mettler Toledo MX5 Microbalance (sensitivity: 0.01 mg) was used to measure the mass of electrode (substrate + MoO_3 nanostructures) and of bare substrate to estimate the MoO_3 mass loading (1.5 mg/cm^2).

The electrochemical measurements were carried out by using a VersaSTAT 4 potentiostat, (Princeton Applied Research, USA) at room temperature, and a three-electrode setup with a Pt

wire as counter electrode, a saturated calomel electrode (SCE) as reference, and the MoO_3 NWs onto GP as working electrode, in 1 M KOH supporting electrolyte. The measured electric current is normalized to the geometrical immersed surface area of the active material, and the potential values are reported vs the reversible hydrogen electrode (RHE), to directly evaluate the OER activity regardless on the pH and the electrolyte. The conversion is carried out according to the Nernst equation [12, 13]:

$$E'_{RHE} = E^{\Theta}_{SCE} + E_{SCE} * 0.059 * pH \quad (1)$$

where E^{Θ}_{SCE} is the standard potential of the SCE electrode at 25°C (0.241 V) and E_{SCE} is the measured potential vs SCE. Linear sweep voltammetry (LSV) is used to investigate the OER activity of the MoO_3 based electrodes. Analysis is recorded at 5 mV/s from 0 V to 0.65 V vs SCE, and the potential values are manually corrected, thus considering the iR_u compensation as follows:

$$E_{RHE} = E'_{RHE} - iR_u \quad (2)$$

where i is the measured electrode current and R_u [Ohms] is the uncompensated resistance, measured by electrochemical impedance spectroscopy (EIS) [14], performed in a potentiostatic mode from 10^5 to 10^{-1} Hz with an AC voltage of 5 mV at the potential (vs SCE) at 10 mA/cm^2 in the LSV curves. Overpotential (η) at fixed current density (typically 10 mA/cm^2) is the most frequently used parameter for the comparison of the OER activity of different electrodes. It is defined as the additional potential (thus considering the iR_u correction) required to sustainably drive an electrochemical reaction from its reversible potential (1.23 V vs RHE in case of OER) [14]. It is determined from polarization curve as follows:

$$\eta = E_{RHE} - 1.23\ V \quad (3)$$

The Tafel slope is extrapolated from the polarization curve, and it is defined by the slope of the linear fit of the potential vs log(j(mA/cm^2)) plot, in an appropriate potential region, chosen to ensure that the measured current density results only from faradaic reaction which occurs during the OER mechanism [15]. It is defined by the following equation [15]:

$$\eta = b * \log(j) + a \quad (4)$$

where η is the iR_u-free overpotential (V), b is the Tafel slope (V/dec), J is the current density (mA/cm^2) and a is a constant.

MoO_3 NWs growth and electrode preparation for electrochemical investigation are reported in Scheme 1.

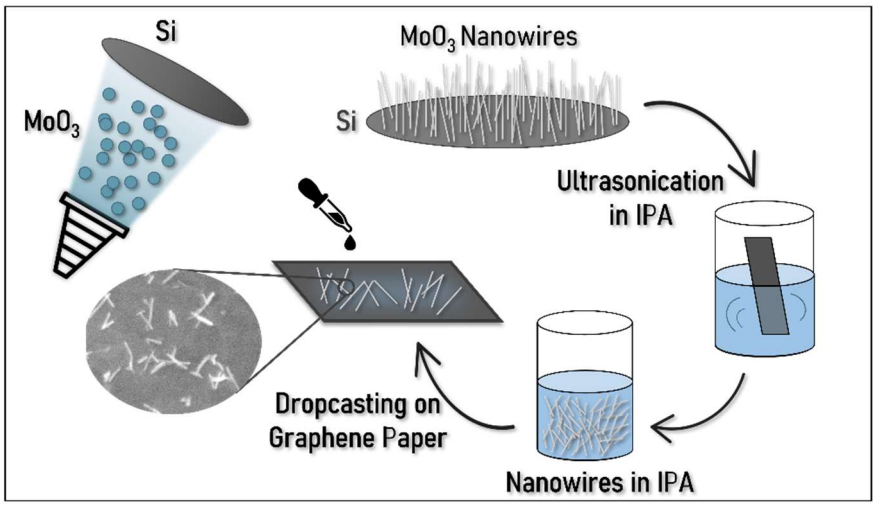

Scheme 1: Illustration of the MoO_3 NWs growth and the electrode preparation processes.

2. Results

MoO_3 was deposited by means of an effusion cell on Si(100) substrates at 200°C, 300°C and 400°C and on Si(111) substrate at 400°C, as described in Materials and Methods section. During the deposition the substrate surface was observed by RHEED and the pattern changed very fast after few minutes. The RHEED patterns before and after deposition at 400°C for the two substrates are reported in Figure S1.

In the case of Si(100) the initial pattern was a well reconstructed 2×1 surface (Figure S1a), indicating a clean surface without native oxide. During deposition, for all the growth temperatures in the range 200°C-400°C, Si surface pattern disappeared, replaced by a diffuse light background. After few minutes diffraction semicircles appeared, indicating the formation of a polycrystalline structure only for T_{growth}=300°C (not shown) and 400°C (Figure S1b), while for the deposition at 200°C only diffuse light was observed till the end of the deposition process.

In the case of Si(111) a 7×7 surface reconstruction (Figure S1c) was present before the deposition start, then the RHEED pattern changed similarly to the Si(100) substrate, replaced by a diffuse light background after few minutes deposition and, then, by the appearance of diffraction semicircles (Figure S1d). A detailed characterization of the samples is reported in the following sections.

2.1 Role of Substrate Temperature

The morphology of samples was investigated by SEM. A first comparison was performed among samples grown at different temperatures on the same substrate, i.e. Si(100). In Figure 1 we report the plan and cross view of three samples with MoO_3 deposited at (a, d) 200°C, (b, e) 300°C and (c, f) 400°C. For the lowest temperature we observe a 80 nm thick and homogeneous film with a flat surface; when temperature is increased up to 300°C a compact bidimensional film is formed, with short nanowires protruding out of it a . At 400°C very thin and straight nanowires are formed, with a diameter of 10-15 nm, and with length depending on the deposition time. In particular, in Figure 1c and 1e the images refer to a sample with about 400 nm long NWs.

The reason why nanowires grow instead of flat islands depends on the existence of favored growth directions, due to different stabilities of low-indexed surfaces with respect to high -indexed surfaces. A similar mechanism is well explained by Zhang et al. [16] *w*ho observed that the V-S growth shows an oscillatory mass transport on the nanowire tip. They describe the process as the simultaneous nucleation of a new atomic layer and the consumption of the rim edge by mass transport to the newly formed step. The mass transport from the rim to the forming atomic layer is finished in a lower time than the one taken by the growth of the rim corner, leading to the formation of NWs.

However, growth temperature can affect the mass transport and, consequently, also the growth rate towards the different directions. This determines a different morphology of the grown structures. In our case we observe a flat bidimensional film for low temperature growth and NWs formation at higher temperature, with an intermediate situation at intermediate temperature, in agreement with the above-described mechanism.

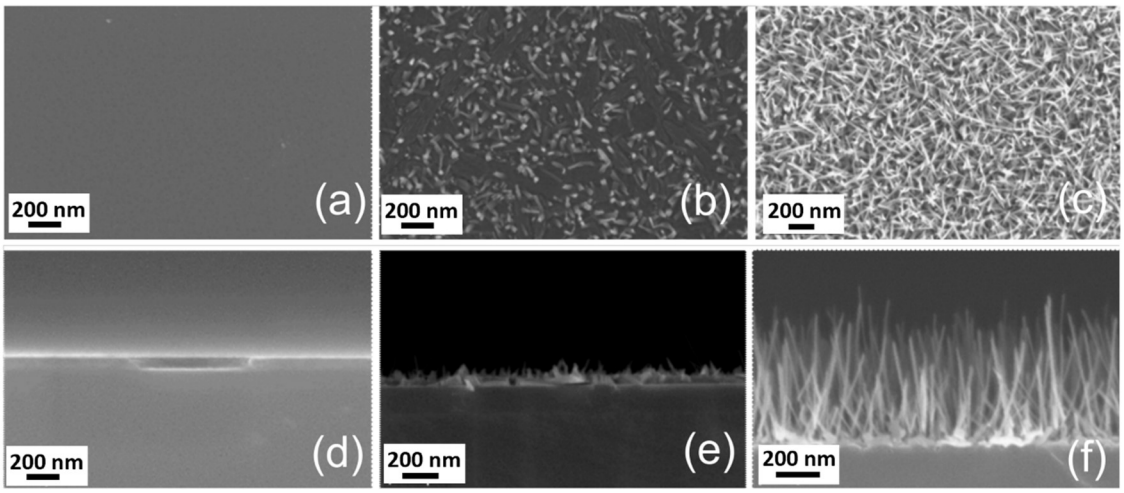

Figure 1: Plan and cross view SEM images of molybdenum oxide grown on Si(100) substrates at different temperatures: (a, d) 200°C, (b, e) 300°C, (c, f) 400°C

The elemental composition of the samples was investigated via RBS. An example of RBS spectrum (precisely for the sample grown on Si(100) at 400°C) is shown in Figure S2 of Supporting Information (SI).

The molybdenum signal is well evident at high energies, while the signal related to oxygen lays above a background due to the silicon substrate. Integrating the peak areas and normalizing them by the RBS yield specific for each element, it was possible to evaluate O and Mo doses (at/cm^2) as well as to estimate the oxide stoichiometry (O/Mo ratio). While the stoichiometry is ≈3 for all the samples, within the measurement error, hence preserving the composition of the source material, the total dose of deposited molybdenum oxide differs from one sample to another: more specifically, the sample grown at 200°C, resulting into a flat and homogeneous film, yields the highest dose, while both the samples grown at 300°C and 400°C on Si(100) substrates show a lower dose. This evidence suggests that the total areal density of deposited material depends on the growth temperature, as reported in Figure S3 of Supporting Information (SI).

Samples deposited on Si(100) at 200°C, 300°C and 400°C were also characterized by XRD analysis and the results are reported in Figure 2.

The XRD pattern confirms the amorphous nature of the sample grown at 200°C, as was already suggested by the observation of RHEED pattern. For the sample grown at 300°C XRD analysis shows diffraction patterns with characteristic peaks at 2θ= 12.84°, 23.67°, 25.84°, 27.41°, 33.67°, 39.13°, which can be attributed to the diffraction from (001), (10-1), (002), (011), (110), (102) lattice planes of the meta-stable monoclinic phase of molybdenum oxide (β-MoO_3) (JCPDS # 047-1320). Similar β-MoO_3 nanostructures were reported [8] for a deposition temperature of 350°C using a system comparable to the one used in our work. In such β phase, MoO_6 octahedra share a corner, preventing the common stratification of α-MoO_3 [17].

For samples grown on Si (100) at the temperature of 400°C, the diffraction peaks match the ones of the thermodynamically stable orthorhombic phase of molybdenum trioxide (α-MoO_3) [17]. In such phase MoO_6 octahedra form double layers bound together by Van del Waals forces, consequently the characteristic peaks visible at 2θ=12.67°, 23.27°, 25.65°, 27.25°, 38.92° are related to the diffraction from lattice planes (020), (110), (040), (021), (060) (JCPDS # 001-0706). Moreover, the diffraction peaks at 22° and 28.6° point out the presence of sub-stoichiometric molybdenum oxide Mo_4O_{11} (JCPDS # 005-0337).

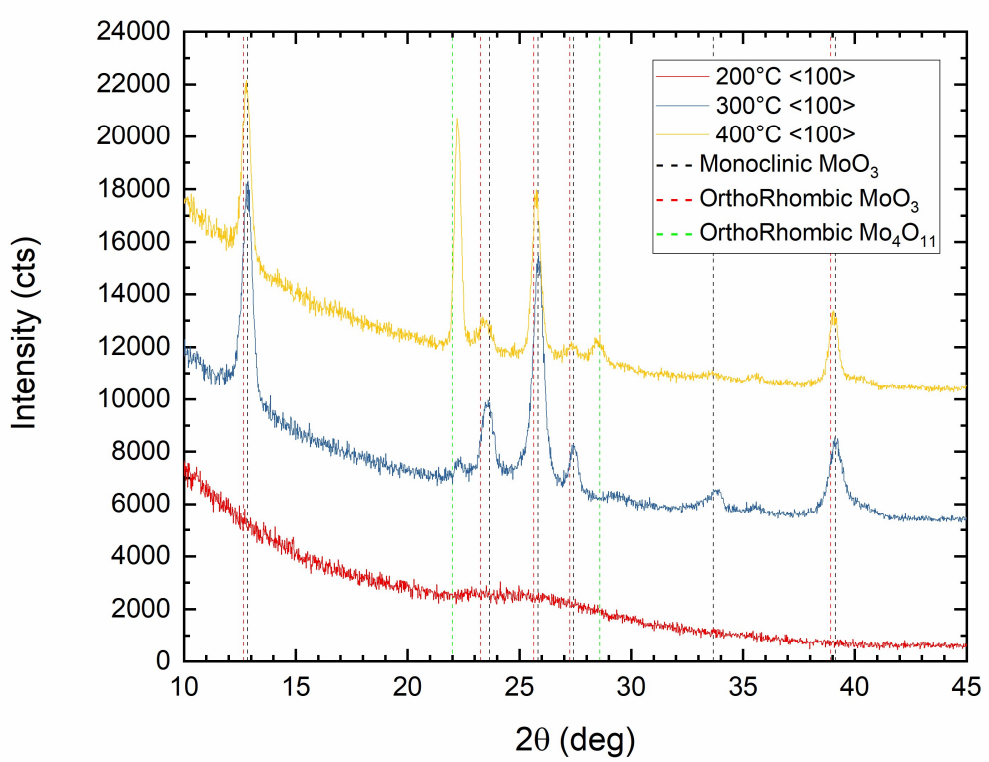

Figure 2: XRD patterns of MoO_x material grown on Si(100) substrate at 200°C (red line), 300°C (blue line) and 400°C (yellow line). Dotted lines indicate the peaks positions associated to the different structures (monoclinic MoO_3, orthorhombic MoO_3, orthorhombic Mo_4O_{11}, according to JCPDS # 047-1320, JCPDS # 001-0706, JCPDS # 005-0337)

For the same sample grown at 400°C STEM analysis was performed. In Figure 3 we report a High-Angle Annular Dark-Field (HAADF) STEM micrograph of a portion of a NW in the foreground (a) along with an enlarged view at high-resolution showing the crystal lattice (b). From this last image the planar distances (0.39 nm along the length direction and 0.18 nm across the width of the NW) were measured. These data match with the (100) and (012) planes of the orthorhombic MoO_3 (space group Pnma) in accordance with what found by XRD analysis. In addition, the [100] growth direction was recognized.

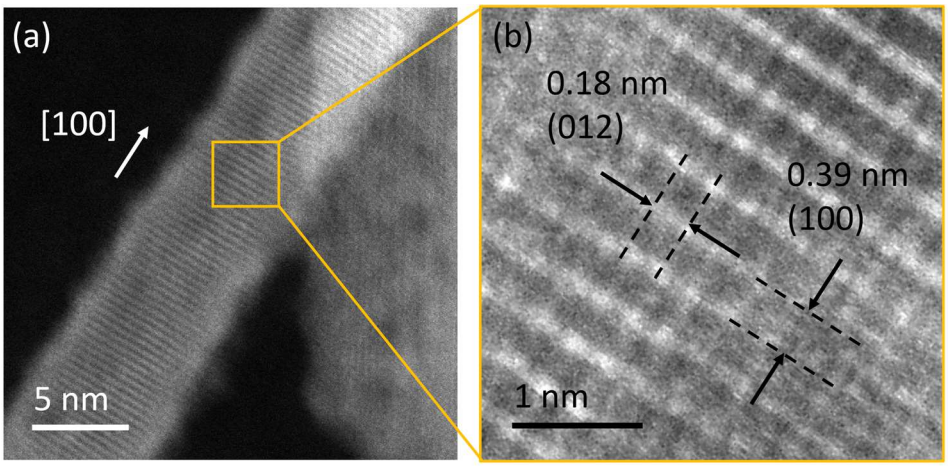

Figure 3: STEM HAADF micrographs of a MoO_x NW portion grown on Si(100) substrate at 400°C (a) and an enlarged view (b)

2.2 Role of Substrate

Once the temperature value was optimized for the MoO_3 NWs growth, the role of the substrate was also investigated. Therefore, we have fixed the growth temperature at 400°C and used two different substrates Si(100) and Si(111). From RHEED analysis (Figure S1) we know that for both surfaces the deposited material has a polycrystalline nature.

SEM analysis was performed in plan and cross section, reported in Figure 4a, b and Figure 4e, f, respectively. The presence of very thin and dense nanowires was observed for both Si(100) and Si(111) substrates; however, in the case of Si(111) additional nanostructures similar to flakes are observed on the surface below and between the nanowires. The difference is clearly visible by comparing images of Si(100) and (111) substrates at higher magnification reported in Figure 4c and d, respectively. Furthermore, due to the formation of both flakes and NWs, the length of the NWs grown on Si(111) is reduced with respect to the case where only NWs grow.

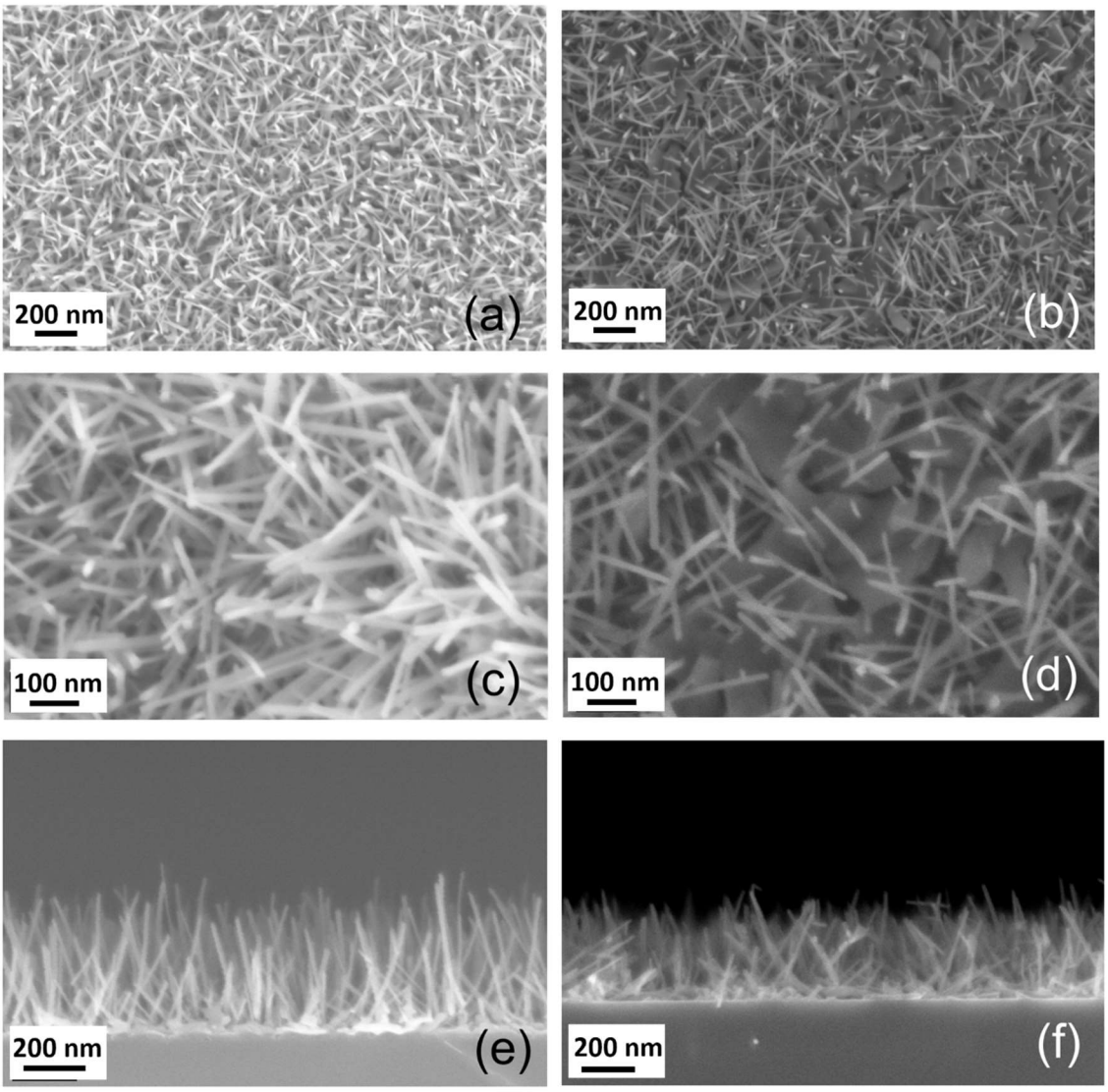

Figure 4: SEM images of MoO_x NWs deposited at 400°C in plan at two magnifications and in cross section on different substrates: (a, c, e) Si(100); (b, d, f) Si(111).

The growth of NWs was also investigated as a function of time for both substrates to observe the nucleation and the evolution of the nanostructures. This experiment was performed by interposing a shutter between the MoO_3 source and the substrate at times t1 and t2, in such a way that one region of the substrate was exposed to the MoO_x flux for the entire deposition time (t3), another region was exposed for few minutes (t1) and another one was exposed for about half the deposition time (t2). In this way SEM investigation provides us the surface situation "frozen" at three different deposition times on the same substrate. In Figure 5 we report the SEM images

showing nucleation and time evolution steps of the nanostructures on (a, c, e) Si(100) and (b, d, f) Si(111) substrates at 400°C.

For Si(100) substrates after a few minutes of deposition (t1) it is possible to observe some small nucleation clusters having a size of 10-15 nm from which NWs start to grow. Both length and density increase as a function of time.

In the case of Si(111) the Mo oxide nucleation looks different with respect to the Si(100) substrate: besides small clusters (nucleation points of NWs) we also observe other flat and hundreds nm large structures. Two of them are indicated by a red arrow in Figure 5d. The size and the surface density of such flakes increase with time, as well as the NWs' one.

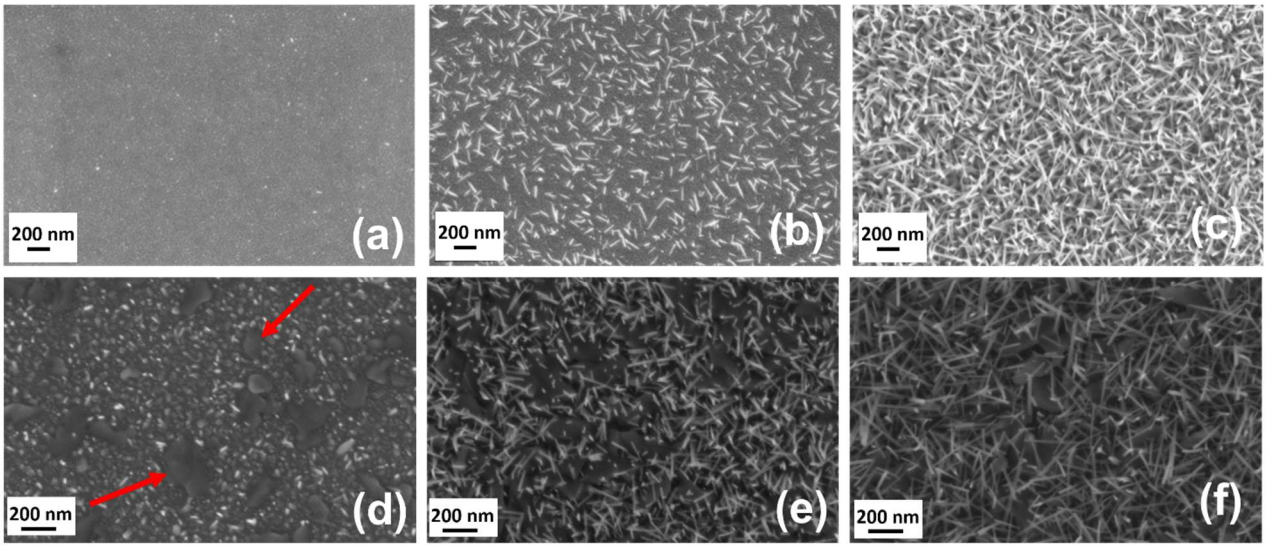

Figure 5: Growth of MoO_3 NWs on (a, b, c) Si(100) and (d, e, f) Si(111) substrates at 400°C, for different deposition times ($t_1<t_2<t_3$)

RBS spectrum acquired for the sample grown at 400°C on Si(111), data not shown here, indicates a O/Mo ratio (2.95±0.16) similar to the ones obtained for the sample grown on Si(100), within the measurement error, furtherly confirming the MoO_3 stoichiometry of the deposited material.

XRD investigation was also performed on sample grown at 400°C on Si(111) substrate. The comparison between XRD patterns for the two samples grown at 400°C on the two substrates is reported in Figure S4 (Supporting information). The two diffractograms show that the main crystalline phase is the orthorhombic α-MoO_3, with the typical 020, 040 and 060 peaks, while the diffraction peaks at 22° and 28.6°can be associated to 211 and 302 lattice planes of the Mo_4O_{11}

orthorhombic phase (JCPDS # 005-0337)]. All the peaks are less intense for the NWs grown on Si(111) substrate with respect to the other sample, due to the different heights of the NWs, as observed by SEM analysis (Figure 4).

As previously done for sample grown on Si(100), STEM analysis on sample grown on Si(111) at 400°C was performed. In Figure 6 we report a STEM HAADF micrograph of a portion of two NWs (a) along with an enlarged view of one NW at high-resolution showing the crystal lattice (b). From this last image the planar distances (0.39 nm along the length direction and 0.33 nm across the width of the NW) were measured. These data match with the (100) and (021) planes of the orthorhombic MoO_3 (space group Pnma) in agreement with what found by XRD analysis. Comparing these results with those obtained for the nanowires grown on the Si(100) substrate, it is evident that in both cases, the wires grow along the [100] direction.

The other structures (flakes) observed by SEM only on Si(111) substrate could not be found and analyzed by TEM/STEM, due to the low amount present on the surface with respect to NWs and lower ease of detaching from the substrate.

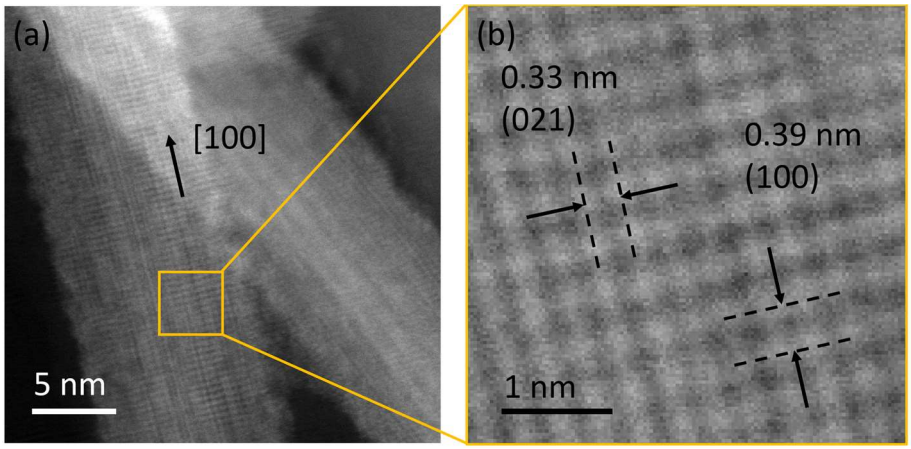

Figure 6: STEM HAADF micrographs of a MoO_x NW portion grown on Si(111) substrate at 400°C (a) and its enlarged view (b)

2.3 Electrochemical activity and OER

To measure the electrochemical activity of MoO_3 nanowires towards the OER, electrochemical analyses were carried out in alkaline media (1 M KOH, pH 14). To this aim, we have selected α-MoO_3 NWs grown at 400°C on Si(100) and on Si(111) substrates, since the density of NWs obtained at 300°C was much lower and, furthermore, they were embedded in a bidimensional layer, making the detachment from the substrate less easy. Figure 7a shows the iR_u-corrected LSV curves reported

versus the RHE scale (eqs. 1 and 2) of the MoO_3-based electrode prepared using NWs grown on a Si(100) and Si(111) substrates (the procedure is reported in Materials and Methods section). In both cases, the current density rapidly increases after an initial stabilization region, due to the pronounced O_2 production, with a high current density at moderate low positive potential, revealing a good electrochemical OER activity with an overpotential at 10 mA/cm^2 (η_{10}) of 340 and 330 mV for NWs obtained from the Si(100) and Si(111) substrates respectively. To deeply analyze the electrocatalytic activity of the MoO_3-based electrode, the polarization curves reported in Figure 7a are further examined by extrapolating the Tafel plots (overpotential η as a function of the logarithmic of the current, Figure 7b). According to the Eq. 4, the Tafel slopes are estimated from the linear fit of the Tafel plots, thus resulting 58 mV/dec and 48 mV/dec for NWs obtained from the Si(100) and Si(111) substrates respectively. Tafel slope is strictly correlated with the rate determining step (RDS) among the electrochemical steps through which the OER occurs. Under alkaline condition, OER occurs through the following electrochemical reactions [17]:

$$OH^-_{aq} + M \rightarrow M - OH_{ads} + e^- \quad (6)$$

$$M - OH_{ads} + OH^-_{aq} \rightarrow M - O_{ads} + H_2O + e^- \quad (7)$$

$$M - O_{ads} + OH^-_{aq} \rightarrow M - OOH_{ads} + e^- \quad (8)$$

$$M - OOH_{ads} + OH^-_{aq} \rightarrow M + O_{2(g)} + H_2O + e^- \quad (9)$$

Where M represents an adsorption active site on the catalyst surface. According to Begildajeva et al. [18], in both our cases, the found Tafel slopes (58 and 48 mV/dec) indicate that the RDS is compatible with the adsorption of OH^- ions at the surface of the electrode and this result does not depend on the substrate used for the synthesis of MoO_3 NWs. Table 1 shows a comparison of η_{10} and Tafel slope among our MoO_3 NWs based electrodes and literature data on MoO_3 and other metal oxide semiconductor-based electrodes. Our samples show the best catalytic performance towards the electrochemical OER in terms of η_{10} and Tafel slope, despite the absence of further catalyst or engineering processes to improve OER performances, thus confirming the promising catalytic activity of MoO_3 NWs for the electrochemical OER. A significant reduction of overpotential and of Tafel slope opens the route towards large utilization of this electrocatalytic nanomaterial for water splitting applications.

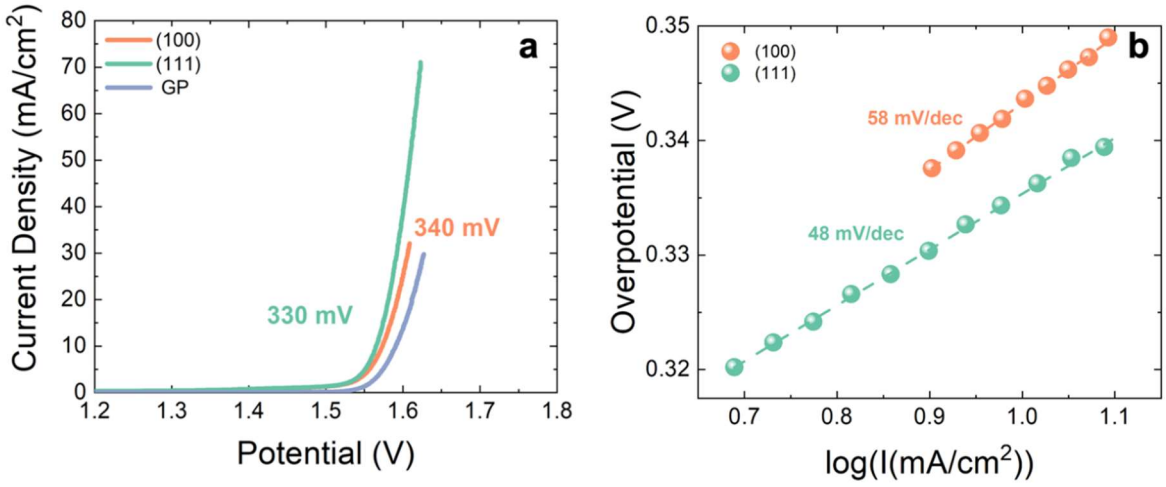

Figure 7: (a) LSV curves obtained in 1 M KOH electrolyte solution at 5 mV/s and (b) Tafel plots (full circles) and linear fit (dotted lines) obtained from the LSV curves of MoO_3 NWs based electrodes obtained from Si(100) and Si(11) substrates (orange and green lines respectively). The LSV curve of bare GP is reported as control sample in panel (a).

To further understand the electrochemical activity difference between MoO_3 NWs obtained from Si(100) and Si(111) the charge transfer kinetics which occurs at the electrode/electrolyte interface is investigated by EIS analysis. Figure 8a shows the Nyquist plots obtained for the MoO_3-based electrodes in 1 M KOH at a potential equal to η_{10}. Beyond the large semicircle, a hint of a very small one can be appreciated at high frequency. The Armstrong circuit (drawn in Figure 8a) is used to model the EIS data. R_u (used for the iR_u compensation of the LSV curve) is related to the resistance at the electrode-electrolyte interface, R_{ct} represents the charge transfer resistance related to the reactions occurring at the substrate-active layer interface, R_p is related to the mass charge resistance of the O_{ads} species on the surface of the active material [19]. C_{dl} and C_p are constant phase capacitances (CPE), described by exponential (n_{dl} and n_p) and pre-exponential (p_{dl} and p_p) factors and are related to the double layer capacitance and pseudo-capacitance, respectively [19]. All fitting values are reported in Table S2 in the SI. For both MoO_3 based electrodes the Nyquist plots show the same trend.

Table 1: Comparison among our MoO_3 based electrodes and literature data on similar nanomaterials.

Structure	**Overpotential (mV)**	**Tafel slope (mV/dec)**	**Electrolyte**	**Ref.**
$Co_{0.5}\,Fe_{0.5}\,WO_4$	524@10 mA/cm^2	36.3	1 M KOH	[20]
$NiO/NiCo_2O_4$	357@10 mA/cm^2	50.3	1 M KOH	[21]
MoO_3	524@100 mA/cm^2	124	1 M KOH	[22]
$Ir_xMo_{1-x}O_d\ (0.1 \leq x \leq 0.5))$	350@10 mA/cm^2	57	0.1 M $HClO_4$	[11]
Orthorhombic MoO_3	370@10 mA/cm^2	65	1 M KOH	[23]
MoO_3 *NWs from Si(100)*	340@10 mA/cm^2	58	1 M KOH	this work
MoO_3 *NWs from Si(111)*	330@10 mA/cm^2	48	1 M KOH	this work

The main difference is related to the R_u parameters, since the NWs obtained from the Si(100) substrate possess a higher R_u than that of NWs obtained from the Si(111) substrate, thus leading to a different iR_u compensation for the polarization curves. This could be due to the different coverage of the GP substrates, since the drop casting method, used for the realization of the electrodes, does not ensure a homogeneous coverage. The R_p and R_{ct} parameters related to the NWs obtained from Si(100) substrate are higher than that of NWs obtained from Si(111) substrate, thus suggesting a certain dependence of the OER mechanism on the average length of NWs. The highest potential drop along the nanostructures is obtained for the longest NWs (obtained from Si(100) substrate), as expected, thus leading to an increase of the R_p and R_{ct} (confirmed by the EIS analysis) and thus justifying the lowest η_{10} obtained for the shortest NWs (grown from Si(111) substrate). The activity per unit of mass (A/mg) at 10 mA/cm^2 versus η_{10} represents a key feature for evaluating the intrinsic catalytic activity of a material towards the OER and for comparing it with that of other materials [24]. Figure 8b shows the performance of our MoO_3 based electrodes (red sphere) in comparison with those of other non-precious metal-based catalysts for alkaline OER (light blue spheres). Our data clearly fits the best performing electrocatalysts, having a quite high mass activity associated with a low catalyst loading (diameter of the circles). Results shown above confirms the possibility to use MoO_3 nanowires grown by thermal evaporation as good electrode for the OER process. Moreover, their

performances can be further improved by doping properly with other elements or by realizing suitable heterostructures, as shown in the literature for metal oxide semiconductors [25, 26].

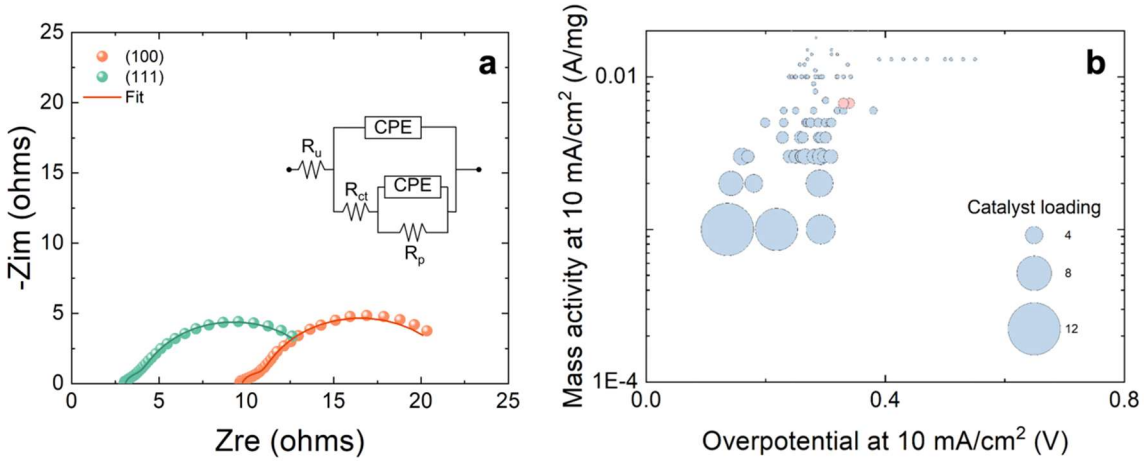

Figure 8: (a) Nyquist plot of the MoO_3-based electrodes, obtained in 1 M KOH electrolyte solution; inset: schematic representation of the Armstrong equivalent circuit. (b) Mass activity at 10 mA/cm^2 as a function of the overpotential at 10 mA/cm^2 of the state of art related to non-precious metal-based catalyst for alkaline OER (light blue spheres, data selected from the list reported as Supplementary information in [24]), and of our MoO_3-based electrodes (red sphere).

2.4 Conclusions

In conclusion, we have reported the growth of α-MoO_3 NWs by thermal evaporation from a stoichiometric MoO_3 source, with the aim of evaluating their use as catalysts for oxygen evolution reaction (OER) in water splitting application. The growth was performed on Si(100) substrates at three different temperatures: 200°C, 300°C and 400°C. At 200°C a flat and amorphous oxide layer is obtained, while as temperature is increased 1D growth prevails on 2D layer formation; in particular at 400°C the deposited material consists of a high density array of MoO_3 crystalline NWs with diameter of a few nm and a length of about 0.5 μm. The growth at 400°C was also performed on a Si(111) substrate, achieving, besides the 1D growth, the formation of small three-dimensional structures (similar to flakes) which precede the formation of the NWs and coexist at the end of the growth. The stoichiometry and the phase of NWs were identified by XRD, RBS and TEM analyses. NWs grown on both Si(100) and (111) at 400°C show the orthorhombic α-MoO_3 phase, while the sample grown at 300°C shows the meta-stable monoclinic phase β-MoO_3.

Finally, α-MoO_3 NWs were deposited on graphene paper and their electrochemical activity was investigated and compared to other non-precious metal-based catalysts for alkaline OER. Our

MoO_3 based electrodes showed overpotentials at 10 mA/cm^2 which ranges between 330 and 340 mV, depending on the length of the MoO_3 nanowires, and a quite high mass activity associated with a low catalyst loading, thus fitting the best performing electrocatalysts.

Our results demonstrate that stoichiometric MoO_3 NWs grown by thermal evaporation are a suitable candidate for the development of anode electrodes for water splitting application.

Acknowledgements

The authors thank G. Malandrino (Università di Catania, Italy) for assistance in XRD analysis. G. Pantè and C. Percolla (CNR-IMM) are acknowledged for technical support.

Author Contributions

The manuscript was written through contributions of all authors. All authors have given approval to the final version of the manuscript.

Supporting Information.

Figure S1: RHEED pattern of (a) 2×1 reconstructed Si(100) surface before deposition; (b) Si(100) substrate at the end of MoO_3 deposition at T_{growth}=400°C; (c) 7×7 reconstructed Si(111) surface before deposition; (d) Si(111) substrate at the end of MoO_3 deposition at T_{growth}=400°C

Figure S2: RBS spectrum of MoO_x material grown on Si(100) substrate at 400°C. The asymmetric shapes of the peaks toward lower energies highlight high roughness, i.e. strong disuniformity of the thickness, caused by the nanostructures.

Figure S3: Total areal density and O/Mo ratio evaluated via RBS spectra of molybdenum oxide samples, grown on Si(100) at 200°C, 300°C and 400°C.

Figure S4: XRD patterns of MoO_3 NWs grown at 400°C on Si(100) and Si(111) substrates. Dotted lines indicate the peaks position associated to the different structures (monoclinic MoO_3, orthorhombic MoO_3, orthorhombic Mo_4O_{11}, according to JCPDS # 047-1320, JCPDS # 001-0706, JCPDS # 005-0337)

References

[1] Xiao, X.; Song H.; Lin S.; Zhou Y.; Zhan X.; Hu Zt.; Zhang Q.; Sun J.; Yang B.; Li T.; Jiao L.; Tang J.; Gogotsi Y.. Scalable salt-templated synthesis of two-dimensional transition metal oxides. *Nature Communications* **2016***,* 7, 11296,DOI: 10.1038/ncomms11296

[2] Borah D. J.; Mostako A. T. T.; Borgogoi A. T.; Saikia P. K.; Malakar A. Modified top-down approach for synthesis of molybdenum oxide quantum dots: sonication induced chemical etching of thin films. *RSC Adv*. **2020**, 10, 3105, DOI: 10.1039/c9ra09773b

[3] Mahmood M.; Chaudhary K.; Shahid M.; Shakir I.; Agboola P. O.; Aadil M. Fabrication of MoO3 Nanowires/MXene@CC hybrid as highly conductive and flexible electrode for next-generation supercapacitors applications. *Ceram. Int.* **2022**, 48 (13), 19314-19323, DOI: 10.1016/j.ceramint.2022.03.226

[4] He X.; Zhang H.; Zhao X.; Zhang P.; Chen M.; Zheng Z.; Han Z.; Zhu T.; Tong Y.; Lu X. Stabilized Molybdenum Trioxide Nanowires as Novel Ultrahigh-Capacity Cathode for Rechargeable Zinc Ion Battery. *Adv. Sci.* **2019**, 6, 1900151, DOI: 10.1002/advs.201900151

[5] Samdani K. J.; Joh D. W.; Rath M. K.; Lee K. T. Electrochemical mediatorless detection of norepinephrine based on MoO_3 nanowires. *Electrochim.Acta* **2017**, 252, 268–27, DOI: 10.1016/j.electacta.2017.08.187

[6] Zhou J.; Xu N.-S., Deng S.-Z.; Chen J.; She J.-C.; Wang Z.-L. Large-Area Nanowire Arrays of Molybdenum and Molybdenum Oxides: Synthesis and Field Emission Properties. *Adv. Mat.* **2003**, 15 (21), 1835-1840, DOI: 10.1002/adma.200305528

[7] Rackauskas S.; Nasibulin A. G. Nanowire Growth without Catalysts: Applications and Mechanisms at the Atomic Scale. *ACS Appl. Nano Mater.* **2020**, 3, 7314−7324, DOI: 10.1021/acsanm.0c01179[8] Maiti P.; Guha P.; Singh R.; Dash J. K.; Satyam P. V.. Optical band gap, local work function and field emission properties of MBE grown β-MoO_3 nanoribbons. Appl. Surf. Sci. **2019**, 476, 691-700, DOI: 10.1016/j.apsusc.2019.01.124

[9] Grimaud A.; Diaz-Morales O.; Han B.; Hong W. T.; Lee Y.-L.; Giordano L.; Stoerzinger K. A.: Koper M. T.M.;Shao-Horn Y. Activating lattice oxides to catalyse oxygen evolution. Nat. Chem. **2017**, 9, 457-465, DOI: 10.1038/nchem.2695

[10] Tahir M.; Pan L.; Idrees F.; Zhang X.; Wang L.; Zou J.-J.; Wang Z. L.Electrocatalytic oxygen evolution reaction for energy conversion and storage: a comprehensive review. *Nano Energy* **2017**, 37, 136-157, DOI: 10.1016/j.nanoen.2017.05.022

[11] Avani A.V.; Anila E.I. Recent advances of MoO_3 based materials in energy catalysis: Applications in hydrogen evolution and oxygen evolution reactions, Int. J. of Hydr. En. **2022**, 47 (47), 20475-20493, DOI: 10.1016/j.ijhydene.2022.04.252

[12] Van Nguyen, T.; Do, H. H.; Tekalgne, M.; Van Le, Q.; Nguyen, T. P.; Hong, S. H.; Cho, J. H.; Van Dao, D.; Ahn, S. H.; Kim, S. Y. WS_2–WC–WO_3 Nano-Hollow Spheres as an Efficient and Durable Catalyst for Hydrogen Evolution Reaction. *Nano Converg.* **2021**, *8* (1):28, DOI 10.1186/s40580-021-00278-3

[13] Yang, M.; Li, J.; Ke, G.; Liu, B.; Dong, F.; Yang, L.; He, H.; Zhou, Y. WO3 Homojunction Photoanode: Integrating the Advantages of WO3 Different Facets for Efficient Water Oxidation. *J. Energy Chem.* **2021**, *56*, 37–45, DOI: 10.1016/j.jechem.2020.07.059

[14] Anantharaj, S.; Ede, S. R.; Karthick, K.; Sam Sankar, S.; Sangeetha, K.; Karthik, P. E.; Kundu, S. Precision and Correctness in the Evaluation of Electrocatalytic Water Splitting: Revisiting Activity Parameters with a Critical Assessment. *Energy Environ. Sci.* **2018**, *11* (4), 744–771. DOI: 10.1039/c7ee03457a

[15] Li, G.; Anderson, L.; Chen, Y.; Pan, M.; Abel Chuang, P. Y. New Insights into Evaluating Catalyst Activity and Stability for Oxygen Evolution Reactions in Alkaline Media. *Sustain. Energy Fuels* **2018**, *2* (1), 237–251, DOI: 10.1039/c7se00337d

[16] Zhang, Z.; Wang, Y.; Li, H.; Yuan, W.; Zhang, X.; Sun, C.; Zhang, Z. Atomic-Scale Observation of Vapor−Solid Nanowire Growth via Oscillatory Mass Transport. *ACS Nano* **2016**, 10 (1), 763−769, DOI: 10.1021/acsnano.5b05851[17] Alves de Castro I.; Shankar Datta R.; Ou J. Z.; Castellanos-Gomez A.; Sriram S.; Daeneke T.; Kalantar-zadeh K.; Molybdenum Oxides – From Fundamentals to Functionality, *Adv. Mater.* **2017**, *29*, 1701619, DOI: 10.1002/adma.201701619

[18] Begildayeva, T.; Chinnadurai, D.; Lee, S. J.; Yu, Y.; Song, J. K.; Choi, M. Y. Implementation of Novel Pulsed Laser Ablation Strategy to Control the Morphological Growth and Enrich the Electrochemically Active Sites of Multifunctional Ni–CuO Electrocatalyst. *J. Alloys Compd.* **2022**, *901*, 163446, DOI: 10.1016/j.jallcom.2021.163446

[19] Krstajić, N.; Popović, M.; Grgur, B.; Vojnović, M.; Šepa, D. On the Kinetics of the Hydrogen Evolution Reaction on Nickel in Alkaline Solution - Part I. The Mechanism. *J. Electroanal. Chem.* **2001**, *512* (1–2), 16–26. DOI: 10.1016/S0022-0728(01)00590-3

[20] Nakayama M.; Takeda A.; Maruyama H.; Kumbhara V.; Crosnier O. Cobalt-substituted iron-based wolframite synthesized via polyol route for efficient oxygen evolution reaction. *Electrochem. Commun*. **2020**, 120, 106834. DOI: 10.1016/j.elecom.2020.106834

[21] Zhang Z.; Liang X.; Li J.; Qian J.; Liu Y.; Yang S.; Wang Y.; Gao D.; Xue D. Interfacial Engineering of $NiO/NiCo_2O_4$ Porous Nanofibers as Efficient Bifunctional Catalysts for Rechargeable Zinc−Air Batteries. *ACS Appl. Mater. Interfaces* **2020**, 12, 19, 21661–21669, DOI: 10.1021/acsami.0c03672

[22] Li X.; Wang Y.; Wang J.; Da Y.; Zhang J.; Lim L.; Zhong C.; Deng Y.; Han X.; Hu W. Sequential Electrodeposition of Bifunctional Catalytically Active Structures in MoO_3/Ni–NiO Composite Electrocatalysts for Selective Hydrogen and Oxygen Evolution, *Adv. Mat.* **2020**, 32(39) , 2003414, DOI: 10.1002/adma.202003414

[23] Jansi Rani B.; Ravi G.; Yuvakkumar R.; Ameen F.; AlNadhari S.; Hong S.I. Fabrication and electrochemical OER activity of Ag doped MoO_3 nanorods, *Materials Science in Semiconductor Processing*, **2020** 107, 104818, DOI: 10.1016/j.mssp.2019.104818

[24] Kibsgaard, J.; Chorkendorff, I. Considerations for the Scaling-up of Water Splitting Catalysts. *Nat. Energy* **2019**, *4* (6), 430–433. DOI: 10.1038/s41560-019-0407-1

[25] Chandrasekaran S.; Ma D.; Ge Y.; Deng L.; Bowen C.; Roscow J.; Zhang Y.; Lin Z.; Misra R.D.K.; Li J.; Zhang P.; Zhang H. Electronic structure engineering on two-dimensional (2D) electrocatalytic materials for oxygen reduction, oxygen evolution, and hydrogen evolution reactions. *Nano Energy* **2020**, 77, 105080, DOI: 10.1016/j.nanoen.2020.105080

[26] Li X,; Hao X.; Abudul A.; Guana G. Nanostructured catalysts for electrochemical water splitting: Current state and prospects. *J. Mater. Chem. A* **2016**, 4, 11973-12000, DOI: 10.1039/C6TA02334G

Graphic for manuscript